AD-784 753

LASER BEAM INTERACTION. PART II

P. D. Thomas, et al

Lockheed Missiles and Space Company

AD 784 753

Prepared for:

Advanced Research Projects Agency
Army Missile Command

August 1974

This research was supported by the Advanced Research Projects Agency of the Department of Defense and was monitored by the U.S. Army Missile Command under Contract Number DAAH01-74-C-0278.

LASER BEAM INTERACTION – PART II

Final Technical Report

By
P. D. Thomas, H. M. Musal, and
Y. S. Chou

LMSC-D403747 August 1974

ARPA Order Number – 2113
Program Code Number – 2E20
Effective Date of Contract – 19 November 1973
Contract Expiration Date – 15 August 1974
Amount of Contract – $59,700
Project Scientist – P. D. Thomas
Phone Number – (415) 493-4411 Ext. 45264

Fluid Mechanics
Lockheed Palo Alto Research Laboratory
LOCKHEED MISSILES & SPACE COMPANY, INC.
A Subsidiary of Lockheed Aircraft Corporation
Palo Alto, California 94304

CONTENTS

ILLUSTRATIONS

ACKNOWLEDGMENT

The authors are indebted to Ms. H. R. Kirch, who participated in the numerical analyses, programmed the GLIT code, and carried out most of the numerical calculations; and to Dr. R. E. Meyerott, consultant, who guided much of the research performed during the course of the study.

SUMMARY

This report summarizes work performed during the concluding phase of a theoretical investigation into the physics responsible for the initiation and propagation of Laser Absorption Waves that have been observed to form over opaque solid targets irradiated in air by an intense laser beam. The report deals separately with the initiation of subsonic Laser Supported Combustion (LSC) Waves over metal targets irradiated by a CO_2 laser at intensities up to a few MW/cm^2 for times of the order of milliseconds or longer; and with the "prompt" initiation of supersonic Laser Supported Detonation (LSD) Waves by short-pulse irradiation at CO_2 laser intensities of the order of 30 MW/cm^2 or greater. In the former case, we had shown previously that the initiation of subsonic waves is dependent on large-scale vaporization of target material, laser-induced inverse bremsstrahlung heating of the vapor, and subsequent heating of ambient air by thermal reradiation from the heated vapor. Recent refinements of the basic theoretical model are presented herein, and are used as a basis for correlating existing experimental data on LSC wave formation.

Two mechanisms that could be responsible for prompt initiation of laser-supported absorption waves in air at CO_2 laser beam intensities above about 30 MW/cm^2 have been investigated. These are high-field electron-emission from protrusions on the target surface, and thermionic electron-emission from anomalous patches on the target surface. Calculations of absorption wave initiation time based on a thermally augmented high-field electron-emission model are not inconsistent with experimental measurements; however, the general trend of the experimental data is not well predicted at the lower end of the intensity range near threshold. Calculations of absorption wave initiation time based on the thermionic electron-emission model, with suitably chosen parameters, agree quite well with available experimental data. Either of two widely differing assumptions about the detailed behavior of the intensely-irradiated target surface can lead to the aforementioned thermionic predictions. One is the presence of surface lamina, or

flakes, that are thermally isolated from the underlying material and that are of the order of the electromagnetic skin depth in thickness. The other assumption is that heat conduction into the bulk of the target material is rate-limited, so that the temperature rise due to laser power absorption within the skin-depth layer at very high incident power densities is affected only by the thermal capacity of the material. This is a heretofore uninvestigated phenomenon, which has far-reaching fundamental implications. Under this assumption, the thermionic electron-emission initiation mechanism involves no additional assumptions nor arbitrarily adjustable parameters, but involves only the intrinsic optical and physical properties of the target material.

In addition to the described analyses of laser Absorption Wave Formation physics, we have continued our earlier formulation of an analysis of a two-dimensional subsonic LSC wave propagating along a finite-diameter laser beam. The formulation is used as the basis for an approximate solution that shows the significant effect of radial flow on the wave propagation speed.

Section 1
INTRODUCTION AND SUMMARY OF PREVIOUS WORK

The effort described in this report and in a previously published Midterm Report (Ref. 1) represents the continuation of an earlier theoretical investigation (Refs. 2 and 3) into the physics responsible for the initiation and propagation of Laser Absorption Waves that have been observed to form over opaque solid targets irradiated in air by an intense laser beam (Refs. 4 to 9).

1.1 SUMMARY OF PREVIOUS WORK

The investigation described earlier was aimed primarily at achieving an understanding of the physics of Laser Absorption Wave initiation over metal targets and at developing theoretical models for predicting the initiation phenomena (Refs. 2 and 3). Considerable effort also was devoted to examining the role played by nonequilibrium phenomena in affecting the internal structure and propagation of fully developed Laser Absorption Waves in air.

To describe the initiation process, a simple model of the laser-target interaction was postulated in Ref. 3. The model is based on uniform, bulk vaporization of the target surface, as opposed to nonuniform vaporization such as might occur in the neighborhood of surface imperfections. As illustrated in Fig. 1, the model consists of:

- A layer of vapor that expands away from the surface
- An outer air shock layer produced by the piston effect of the expanding vapor

Estimates of the gasdynamics and of the laser energy transport in the vapor and air layers showed that significant heating of the gas by inverse bremsstrahlung absorption takes place first in the vapor, rather than in the shocked air; and that the subsequent

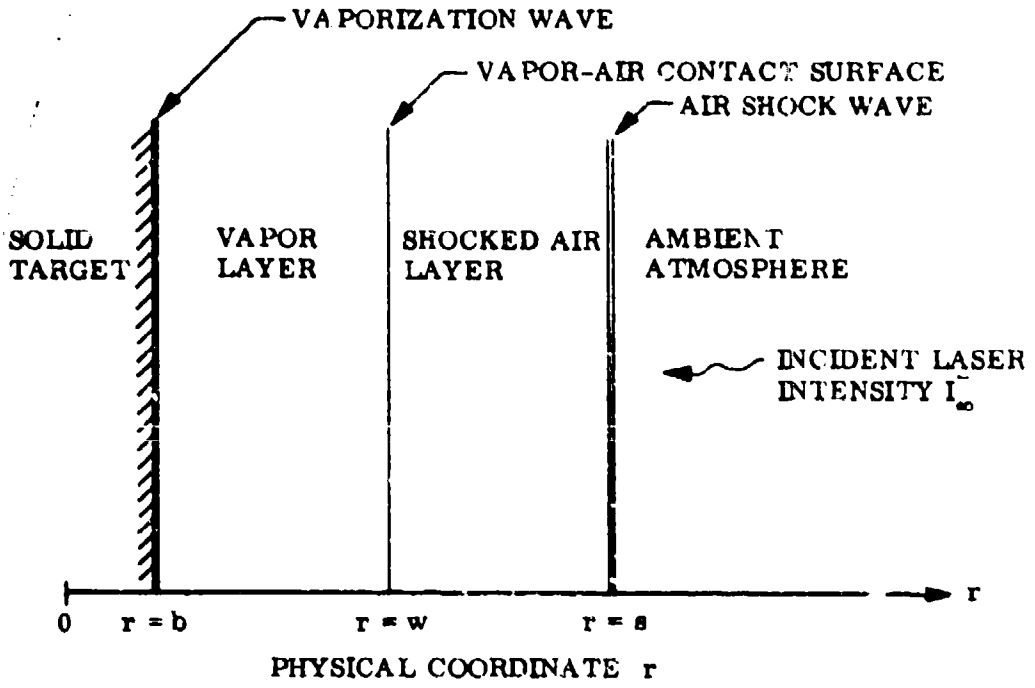

Fig. 1 Diagram of Interaction Region

formation of an absorption wave in the air is connected to this initial heating of the vapor. Nonequilibrium phenomena were examined, and found to play a relatively minor role both in the vapor heating process and in the physics of wave propagation over the laser intensity-wavelength regime where subsonic Laser-Supported Combustion (LSC) waves have been observed experimentally (Refs. 7, 8, 9); namely, for intensities of the order of 10^6 W/cm^2 or less at CO_2 laser wavelength (10.6 μ).

In contrast, it was found that nonequilibrium phenomena are of major importance in the regime where supersonic Laser-Supported Detonation (LSD) waves have been observed (Refs. 4, 5, and 6). Recent computer calculations of LSD wave propagation appear to confirm this conclusion (Ref. 10).

The described uniform vaporization model was used as the basis for detailed analysis of the laser-target interaction (Ref. 2). The analysis is embodied in a computer code called GLIT (Gasdynamics over Laser-Irradiated Targets) that solves the one-dimensional, time-dependent Eulerian gasdynamics equations for both vapor and air layers. The solutions account for heat conduction in the solid target, and for the transport both of laser radiation and of thermal radiation emitted by the gas. Code calculations were performed for the conditions of a typical experiment in which LSC waves were initiated over an aluminum alloy target irradiated by a CO_2 laser at a peak intensity of 2 MW/cm^2. The calculations showed the formation of an incipient LSC wave in the air over the target on a time scale consistent with the experimental observations. The wave initiation mechanism in the calculations was the following: Vaporized target material, heated by inverse bremsstrahlung absorption of laser energy, emits thermal radiation at frequencies that are strongly absorbed by cold air. An absorption wave forms when the air become sufficiently ionized to absorb laser energy directly.

These detailed results, together with additional approximate calculations, indicated that the uniform vaporization model is valid at CO_2 laser wavelength in the regime of intensities of the order of 1 MW/cm^2 or less and laser pulse durations of the order

of 1 ms or longer. However, the model appears inadequate to explain experimental data obtained in short-pulse experiments at intensities between 30 and 300 MW/cm^2. Within this intensity regime, prompt initiation of strong LSD waves was observed to occur in a shorter time scale than that required for the onset of uniform surface vaporization (Refs. 4, 5, and 6). Furthermore, this "prompt" initiation was observed to occur at localized "spots," or sites, that were randomly distributed over the irradiated area of the target surface (Ref. 4). This suggested that additional phenomena were operating in this higher power regime.

Examination of the surface of aluminum sheet stock of the type used in the experimental studies, using a scanning electron microscope, showed localized randomly distributed pits, scratches, protrusions, and inclusions that could be the sites for "prompt" absorption wave initiation (Refs. 2, 4).

Several mechanisms for production of ionization at these sites, from which an absorption wave could evolve, appear possible. One is localized vaporization of inclusions or lamina which may have higher absorptivity than the surrounding metal surface and poor thermal contact with the bulk of the metal. This would lead to a plasma "microjet" of the material. A second mechanism is thermionic emission from "hot spots" associated with surface imperfections. A preliminary evaluation of this possibility was made (Ref. 3), and it was tentatively concluded that low emission yields and space-charge limitations would severely limit the ionization level that could be achieved.

The third mechanism that was considered was localized high-field emission from protrusions on the surface (Ref. 2). It was found that protrusions or sharp edges are required to intensify the normal electric field of the incident laser beam sufficiently to produce a large electron emission yield in the "prompt" initiation laser intensity regime. Furthermore, protrusions of sufficient height distort the field enough to cause the emitted electrons to be accelerated to energies adequate to collisionally ionize the ambient air molecules. This negates the space charge effect and produces an air plasma that subsequently undergoes laser-induced breakdown by cascade

energy and subsequent heating of the air by thermal emission from the vapor occur relatively quickly.

These results suggested that, if the theoretically predicted behavior were true also of the experiments, then it should be possible to correlate all available experimental data as a function of the fundamental parameters that govern the heat-conduction process. Classical heat-conduction theory was used to deduce the fundamental parameters as follows: The GLIT code calculations, in agreement with the experimental measurements for the three cases cited above, predicted the LSC wave formation to occur during the initial risetime of the laser pulse; during this part of the pulse, the incident laser intensity history can be represented by a ramp function $I(t) = \dot{I}t$. Here t denotes the time and $\dot{I}$ = const. is the characteristic slope of the ramp. For an opaque solid target that vaporizes at temperature T_v and that has thermal conductivity k, density ρ, heat capacity C, and surface absorptivity α, the heat-conduction solution leads to the following equation for the time of onset of surface vaporization:

$$t_v = \left[\frac{9\pi}{16} k\rho C \left(\frac{T_v - T_b}{\alpha}\right)^2\right]^{1/3} [\dot{I}]^{-2/3} \qquad (1)$$

where T_b is the initial target temperature prior to irradiation.

It is seen from this equation that the fundamental laser beam parameter that governs heat conduction in the target and that affects the time required to produce vapor is the characteristic slope $\dot{I}$ of the laser pulse. Thus, it was deduced (Ref. 1) that if the behavior predicted by the GLIT code calculations were true of the experiments, then experimentally observed LSC wave initiation times t_i should correlate well when plotted as a function of the average slope of the laser pulse up to the initiation time. For simplicity, the following simple mean value was employed in attempting such a correlation:

$$\langle \dot{I} \rangle = t_i^{-1} \int_0^{t_i} \dot{I}\, dt = I(t_i)/t_i \qquad (2)$$

The correlation is displayed in Fig. 2, which is reproduced from Ref. 1. The figure contains all experimental points for which a self-consistent set of data are available (Refs. 7, 8, 11) including shots for ambient pressures other than 1 atm. For reference, Eq. (1) is plotted as the solid line in Fig. 2. The close correlation among experimental data points in the latter figure is evident. Furthermore, the data follow the trend predicted by Eq. (1), namely, that the LSC wave initiation time varies as $\langle \dot{I} \rangle^{-2/3}$. This is very strong evidence of the fundamental validity of the uniform surface vaporization model and of the basic physics of the LSC wave initiation process that are used in the GLIT code. That is, the generation of a vapor layer is a necessary precondition to the formation of an absorption wave; inverse bremsstrahlung absorption of laser energy takes place in the initially weakly ionized vapor; thermal radiation emitted by the hot vapor then raises the air to temperatures at which it is ionized sufficiently to absorb laser energy directly, and an absorption wave is formed.

In addition to the above studies of absorption wave initiation physics, the Midterm Report (Ref. 1) presented an analysis of a two-dimensional (axisymmetric) subsonic laser absorption wave in air. Preliminary results were obtained that account for the two-dimensional geometry of the LSC wave propagating along a finite-diameter laser beam, with a realistic treatment of the transport of laser radiation and of thermal radiation emitted by the hot gas in the core of the wave.

1.2 OVERVIEW OF THIS REPORT

This report summarizes work performed during the concluding phase of the overall Laser-Target Interaction study described in the opening sentences of the foregoing introduction. In Section 2, we develop some improvements to the correlation of experimental data on subsonic LSC wave formation (Fig. 2). The heat-conduction

$$\langle \dot{I} \rangle = t_i^{-1} \int_0^{t_i} \dot{I}\, dt = I(t_i)/t_i \qquad (2)$$

The correlation is displayed in Fig. 2, which is reproduced from Ref. 1. The figure contains all experimental points for which a self-consistent set of data are available (Refs. 7, 8, 11) including shots for ambient pressures other than 1 atm. For reference, Eq. (1) is plotted as the solid line in Fig. 2. The close correlation among experimental data points in the latter figure is evident. Furthermore, the data follow the trend predicted by Eq. (1), namely, that the LSC wave initiation time varies as $\langle \dot{I} \rangle^{-2/3}$. This is very strong evidence of the fundamental validity of the uniform surface vaporization model and of the basic physics of the LSC wave initiation process that are used in the GLIT code. That is, the generation of a vapor layer is a necessary precondition to the formation of an absorption wave; inverse bremsstrahlung absorption of laser energy takes place in the initially weakly ionized vapor; thermal radiation emitted by the hot vapor then raises the air to temperatures at which it is ionized sufficiently to absorb laser energy directly, and an absorption wave is formed.

In addition to the above studies of absorption wave initiation physics, the Midterm Report (Ref. 1) presented an analysis of a two-dimensional (axisymmetric) subsonic laser absorption wave in air. Preliminary results were obtained that account for the two-dimensional geometry of the LSC wave propagating along a finite-diameter laser beam, with a realistic treatment of the transport of laser radiation and of thermal radiation emitted by the hot gas in the core of the wave.

1.2 OVERVIEW OF THIS REPORT

This report summarizes work performed during the concluding phase of the overall Laser-Target Interaction study described in the opening sentences of the foregoing introduction. In Section 2, we develop some improvements to the correlation of experimental data on subsonic LSC wave formation (Fig. 2). The heat-conduction

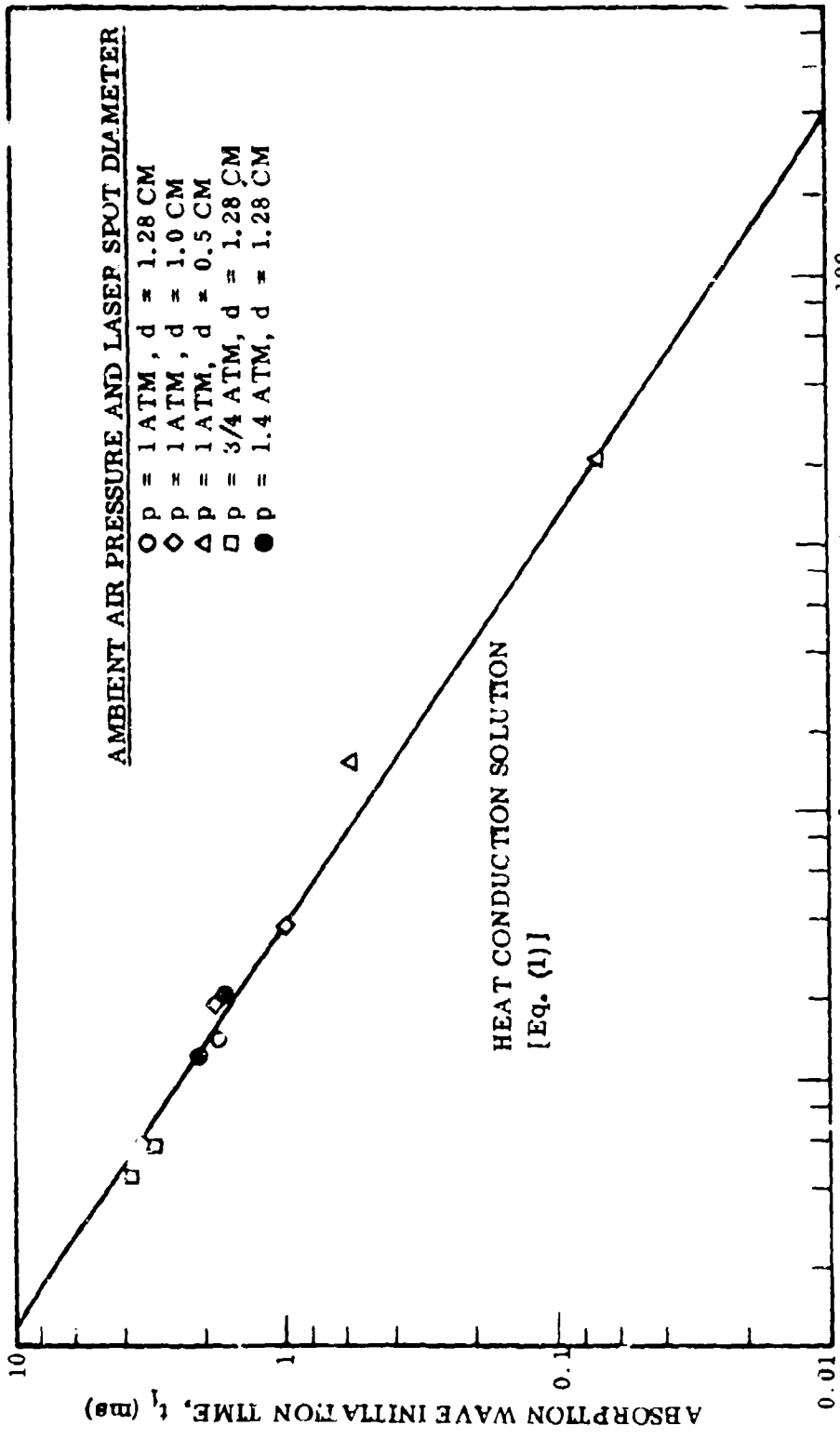

Fig. 2 Correlation of Experimental Data on LSC Wave Initiation Over Titanium Targets (Refs. 7, 8, 11)

solution originally performed for a ramp-function laser pulse is generalized so as to yield a rigorous solution for the laser beam parameter of an arbitrary pulse shape. This includes the singular case where the pulse shape function has integrable discontinuities such as the initial discontinuity that characterizes a step-function pulse.

Section 3 deals with "prompt" absorption wave initiation. Our earlier model based on purely high-field emission from surface protrusions is extended to account for enhancement of the electron emission current by thermionic emission from laser-heated material. In addition, following a recent suggestion by Walters (Ref. 4), we have re-examined in some detail the model based upon purely thermionic emission from a relatively smooth surface for which the field effect is negligible at laser intensities near the threshold for "prompt" LSD wave formation. It is shown that, with this model, either of two widely different assumptions about the physical behavior of the target material under very intense laser irradiation can lead to predictions that agree both qualitatively and quantitatively with the experimental data.

Section 4 presents additional results based on our earlier formulation of an analysis of a two-dimensional subsonic LSC wave propagating along a finite-diameter laser beam. A simplified approximate solution is developed that demonstrates the significant effect of radial flow on the wave-propagation speed.

Section 2
INITIATION OF SUBSONIC LASER ABSORPTION WAVES

As indicated earlier in subsection 1.1, several detailed GLIT code calculations have been performed that are in close agreement with experimental data on subsonic Laser Supported Combustion (LSC) wave initiation over titanium targets irradiated by a CO_2 gas laser at peak intensities below a few MW/cm^2 (Ref. 1). On the basis of the behavior evinced by these theoretical calculations, a large body of such experimental data have been correlated successfully as a function of the fundamental laser beam parameter that governs the thermal response of the laser-irradiated target (see subsection 1.1). Under circumstances where the laser pulse can be approximated by a ramp function, a rigorous target heat conduction solution [Eq. (1)] revealed this fundamental parameter to be the slope of the ramp pulse. However, this solution does not apply directly to cases where the wave was initiated so late in the pulse that the ramp approximation is unjustified. Nevertheless, as shown in Fig. 2 of subsection 1.1, such cases were found to correlate reasonably well as a function of the simple average slope given by Eq. (2). In this section, we develop a rigorous definition of the average slope that is valid for an arbitrary laser pulse shape and apply this result to obtain an improved correlation of the available experimental data.

We begin with the well-known exact heat conduction solution for the surface temperature history of an irradiated solid (Ref. 1):

$$T - T_b = \frac{\alpha}{\sqrt{\pi k \rho C}} \int_0^t \frac{I(t')}{\sqrt{t - t'}}\, dt' \qquad (3)$$

where T_b is the initial temperature and $I(t)$ is the incident laser pulse.

If the latter pulse is a continuous and differentiable function of time, then Eq. (3) may be integrated by parts. The resulting expression then may be solved for the onset of vaporization t_v defined as the time at which the surface reaches its vaporization temperature T_v. The solution is identical to Eq. (2) of subsection 1.1, which applies to a ramp pulse, except that the slope $\dot{I}$ = const. of the ramp is replaced by a weighted average of the time-derivative $\dot{I} = dI/dt$ of the arbitrary pulse

$$t_v = \left[\left(\frac{9\pi}{16} k\rho C \right) \left(\frac{T_v - T_b}{\alpha} \right)^2 \right]^{1/3} \langle\langle \dot{I} \rangle\rangle^{-2/3} \tag{4a}$$

where

$$\langle\langle \dot{I} \rangle\rangle = \frac{3}{2} \int_0^1 (1 - \xi)^{1/2} \dot{I} \, d\xi \quad , \quad \xi = t/t_v \tag{4b}$$

In practice, the laser pulse shape usually can be approximated accurately by a piecewise-linear curve-fit of the form

$$I(t) = \begin{cases} 0 \quad , & t < 0 \\ \dot{I}_1 t \quad , & 0 \le t \le t_1 \\ \sum_{i=1}^{j-1} \dot{I}_i (t_i - t_{i-1}) + \dot{I}_j (t - t_{j-1}) \quad , & t_{j-1} \le t \le t_j \end{cases} \tag{5}$$

where we have defined $t_j = 0$ for $j = 0$. The derivative $\dot{I}$ is then piecewise constant, and the integral that appears in Eq. (4b) can be evaluated readily to yield the following simple analytical expression for the average pulse slope

$$\langle\langle \dot{I} \rangle\rangle = \sum_{j=1}^{k-1} \dot{I}_j \left[(1 - \xi_{j-1})^{3/2} - (1 - \xi_j)^{3/2} \right] + \dot{I}_k (1 - \xi_{k-1})^{3/2} \tag{6}$$

where the integer k is determined uniquely by the condition

$$\xi_{k-1} < 1 \leq \xi_k \tag{7a}$$

or, equivalently,

$$t_{k-1} < t_v \leq t_k \tag{7b}$$

Equation (4b) cannot be used if the laser pulse is either a step-function in time, or is any other function that possesses jump discontinuities at which the derivative $\dot{I}$ does not exist. An example that is of practical interest for currently planned experiments (Ref. 11) is the situation in which the incident pulse is tailored so as to possess a sharp initial jump discontinuity similar to that of a step function. The foregoing analysis can be generalized to apply to the situation by separating the integral that appears in Eq. (3) into two parts

$$\int_0^t \frac{I(t')\,dt'}{\sqrt{t-t'}} = \lim_{\epsilon \to 0} \left\{ \int_0^{\epsilon} \frac{I(t')\,dt'}{\sqrt{t-t'}} + \int_{\epsilon}^{t} \frac{I(t')\,dt'}{\sqrt{t-t'}} \right\}$$

where $0 < \epsilon < t$. Upon evaluating the integrals and taking the $\epsilon \to 0$ limit, one obtains an equation for t_v that is identical to Eq. (4a), except that the average pulse slope is defined as follows [compare Eq. (4b)]:

$$\langle\langle \dot{I} \rangle\rangle = \frac{3}{2} \frac{I(0^+)}{t_v} + \frac{3}{2} \int_{0^+}^{1} (1-\xi)^{1/2} \dot{I}\, d\xi \tag{8}$$

where $I(0^+) \equiv \lim_{t \to 0^+} [I(t)]$ represents the magnitude of the initial jump discontinuity in the laser pulse.

Equations (4b) and (8) represent rigorous definitions of the average laser pulse slope for a pulse of arbitrary shape. We have used these results to improve our earlier correlation (Fig. 2) of experimental data on LSC wave initiation over titanium targets. The results are displayed in Fig. 3, and include two additional data points at large $\langle\langle \dot{I} \rangle\rangle$ that have recently become available (Ref. 11). As one might expect, the two correlations differ significantly only near the lower end of the $\langle\langle \dot{I} \rangle\rangle$ scale, where the observed LSC wave initiation took place relatively late in the pulse.

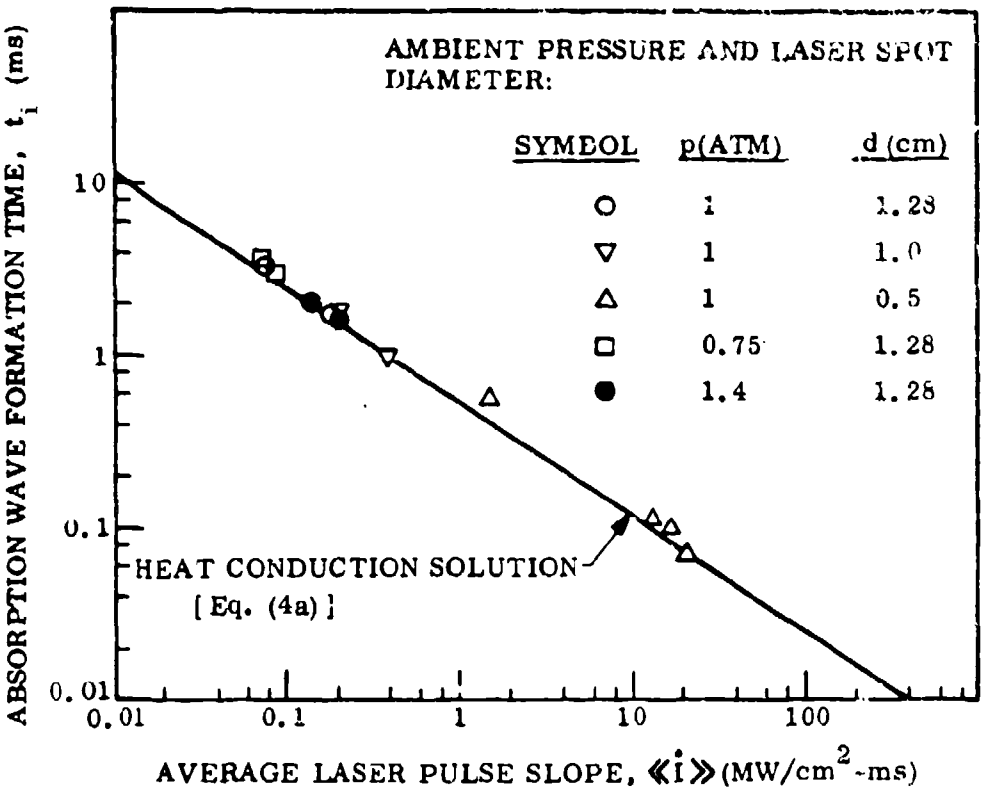

Fig. 3 Correlation of LSC Wave Formation Times as a Function of the Average Laser Pulse Slope Defined in Eq. (4b). MSNW data on titanium targets irradiated by a CO_2 laser (Refs. 7, 8, and 11)

Section 3
PROMPT INITIATION OF SUPERSONIC LASER ABSORPTION WAVES

3.1 GENERAL DISCUSSION

Laser-supported absorption waves are initiated at solid opaque target surfaces in an ambient atmosphere at laser beam intensities below the intrinsic electromagnetic breakdown threshold of the atmosphere. Initiation is accomplished by the emission of free electrons from the surface. These electrons provide the "seeding" for a cascade ionization buildup, which eventually becomes a traveling absorption wave. The mechanism for the production of the initial "seed" electrons varies over the laser beam intensity range of concern in high-power laser applications. At intensities below a few megawatts/cm^2, we have shown in the previous section of this report that vaporized target material appears to be the dominant contributor of the initial free electrons. However, at intensities above 10-MW/cm^2, other faster initial production mechanisms appear to become dominant. Two such mechanisms that we have investigated are high-field electron-emission from protrusions on the target surface, and thermionic electron-emission from anomalous patches on the target surface.

In this section, we present the results of additional modeling and analysis of "prompt" initiation of laser-supported absorption waves in the high-intensity regime (3×10^7 to 3×10^8 W/cm^2). Previously, we modeled this phenomenon as a cascade ionization process in the ambient atmosphere triggered by high-field electron-emission from the target surface under laser beam irradiation (Ref. 1). In this model, there is no thermal time lag involved, because pure high-field electron-emission depends on the instantaneous laser beam intensity and therefore requires no surface temperature rise. However, if the target surface temperature does rise, thermal enhancement of the high-field electron-emission will occur. This extension to the pure field-emission model has been incorporated into our prompt initiation analysis. The results show that if it is assumed that the electron-emitting protrusions are thermally isolated from the

bulk of the surface material, so that their temperature rise is controlled by their thermal capacity rather than by heat conduction to the bulk of the target material, the thermal enhancement effect plays a major role at the lower end of the cited intensity range near the LSD wave formation threshold. However, the high-field effect alone appears dominant at the high end of the cited intensity range. These theoretical results are highly dependent on the geometrical configuration of the surface protrusions. Even with somewhat extreme assumptions about the effective sharpness of the protrusions, the predictions of this model are not entirely satisfactory in terms of agreement with available experimental data.

We have also reexamined the purely thermionic electron-emission mechanism to see whether it offers better theoretical-experimental correlation than does the high-field electron-emission mechanism. An analysis of a model for prompt initiation based on thermionic electron-emission from the target surface and concomitant cascade ionization in the ambient atmosphere has been carried out. In this model it is assumed that the thermionic electron-emission takes place from localized "lamina" (or thin surface layers) that are thermally isolated from the bulk of the target material and that are heated by the incident laser beam. The emitted electrons act as the "seed" for cascade ionization buildup in the ambient atmospheric region over the emitting area. The results of the analysis show that this thermionic emission model, with suitably chosen parameters, can lead to calculated absorption wave formation times that agree quite well with available (Battelle) experimental data. However, here too we must make a somewhat extreme assumption about either the thinness of these lamina or the intrinsic character of the heat-transfer process within the target material at very high heating rates.

3.2 HIGH-FIELD ELECTRON-EMISSION INITIATION MODEL

3.2.1 Model Characteristics

A detailed description and discussion of the model for "prompt" initiation of laser-supported absorption waves via purely high-field electron-emission from protrusions

on the target surface has already been given (Refs. 1, 2) and is summarized in subsection 1.1 of this report. However, a brief review will put the latest contribution into perspective. Figure 4 illustrates the model schematically. A localized protrusion, modeled as a prolate spheroid, stands out from the local "average" target surface. Coherent interference between the incident and reflected laser beams creates a standing-wave electric field that has a component normal to the surface. This field is distorted in the vicinity of the protrusion, so that the normal electric field intensity at the tip of the protrusion is enhanced (by a factor F) above the normal electric field intensity over the "average" target surface. If the electric field intensity at the tip is sufficiently large (of the order of 2×10^7 V/cm), electrons are emitted directly from the tip (high-field electron-emission). These emitted electrons are accelerated as they pass through the high-field region that surrounds the protrusion tip. For protrusion heights less than approximately one-tenth the wavelength of the incident radiation, the kinetic energy that these electrons can gain in traversing this high-field region is given by $E_{no}h$, where h is the protrusion height and E_{no} is the normal component of the standing-wave electric field at the "average" target surface far from the protrusion. At sufficiently high laser beam intensities (above 1×10^7 W/cm^2 for 10.6-μ radiation) and large field-enhancement factors ($F \approx 100$), the emitted electrons gain enough energy to ionize the ambient air by direct impact. This ionization creates an air plasma in the neighborhood of the protrusion. The size of this plasmoid is approximately the "ionization range" of the emitted electrons (typically of the order of 10 μ in air at S.T.P.) The free electrons in this plasmoid then act as the priming electrons for an electron cascade ionization buildup.

In this process, the free electrons absorb energy from the laser beam by inverse bremsstrahlung, thus heating to a temperature high enough so that they create additional ion-electron pairs by inelastic collisions with neutral molecules. This is simply a laser-induced breakdown starting from substantially preionized air, which proceeds much faster than air breakdown starting from usual initial conditions. Eventually, the plasmoid electron density becomes high enough so that most of the intercepted laser energy is absorbed, and the plasmoid then grows explosively. The plasmoid is then the nucleus of an absorption wave. We have assumed in our analysis that the "incubation

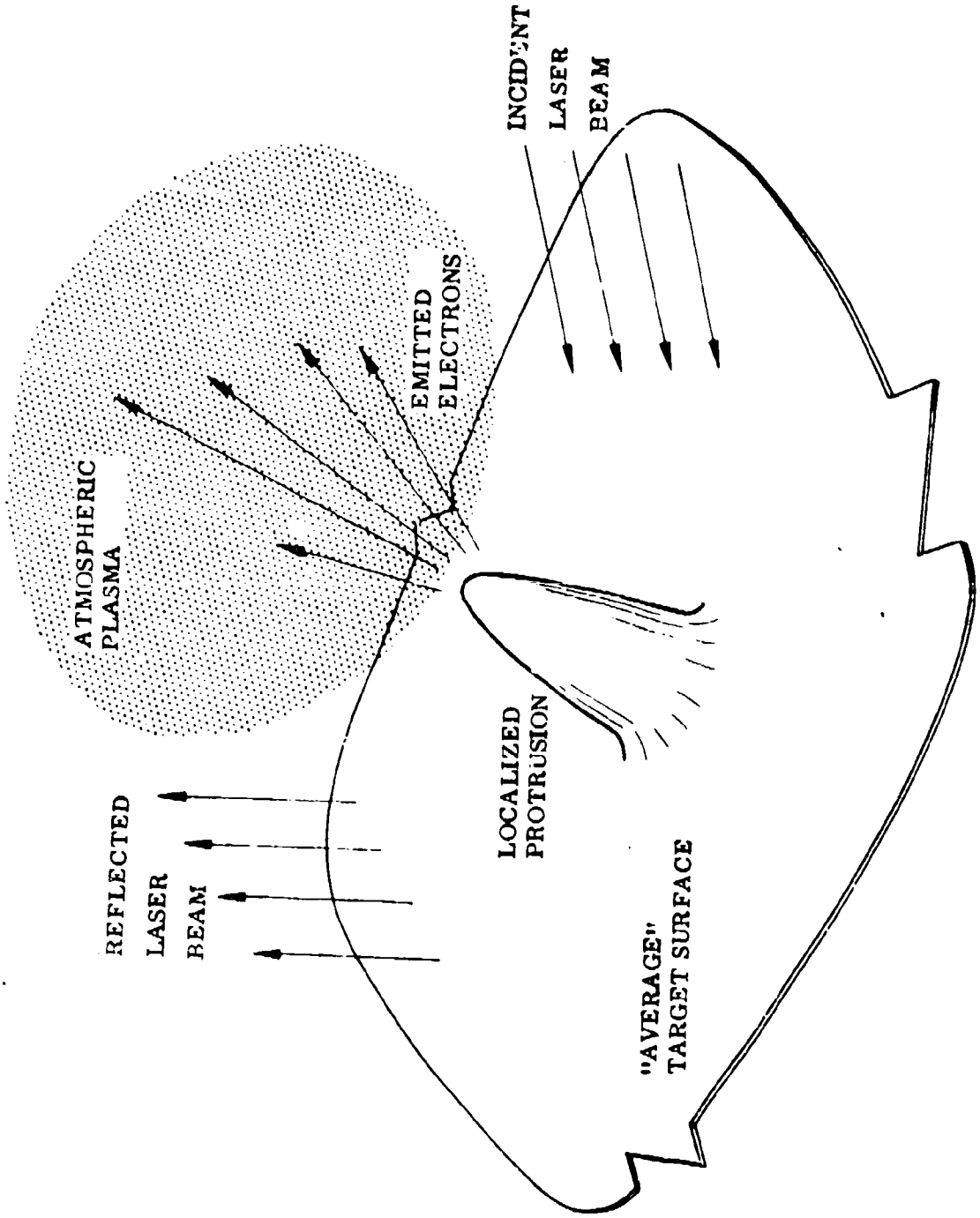

Fig. 4 Localized Plasma Formation at a Surface Protrusion

time" for absorption wave formation is the time required for the electron density in the plasmoid to increase to the critical electron density for the incident laser wavelength.

At the lower end of the laser beam intensity range of concern for prompt initiation of absorption waves (about 3×10^7 W/cm^2 for CO_2 lasers), the time required for the plasmoid electron density to reach critical value via purely high-field electron-emission and concomitant ionization cascade was calculated to be sufficiently long to make it appear that some heating of the surface and protrusion could take place. This would enhance the electron emission, and therefore tend to shorten the incubation time.

In order to incorporate this phenomenon into the prompt initiation model, we have formulated an analytic description of electron emission from a surface protrusion under the condition of simultaneous existence of a very high normal electric field and elevated temperature, and have developed a method for calculating the temperature rise of the protrusion due to laser energy absorption.

The analysis, involving considerations of temperature-field emission, protrusion heating, and the numerical results, is presented in detail below.

3.2.2 Analysis

Temperature-Field Emission. The emission of electrons from a heated surface in the presence of a very high normal electric field is designated as temperature-field (T-F) electron emission (Ref. 12). This is a particularly difficult regime in which to obtain an explicit analytical expression for the electron-emission current density which is needed in our model to calculate the electron density buildup in the plasmoid over an emitting protrusion. Approximations have been developed based on approaches from either the purely high-field regime or the purely thermionic regime (Ref. 13). In the former approximation, only a very small temperature-effect correction can be validly applied to the high-field emission equation. This correction term becomes divergent for temperatures of concern in our calculations. In the latter approximation, the

well-known Richardson-Schottky formula for electric-field-enhanced thermionic emission is obtained. Unfortunately, this formula does not apply at the high electric field intensities of concern in our calculations.

To cover the regime between purely high-field emission and predominantly thermionic emission, we have developed an empirical relationship that asymptotically approaches each limit and provides a smooth transition between them. This equation gives the electron emission current density, J_{TF} (A/cm^2), due to simultaneous high electric field and elevated temperature, in the form

$$J_{TF} \cong K_{TF}\, e^{-k_{TF}} \tag{9}$$

$$K_{TF} \equiv K_T + K_F \tag{10}$$

$$k_{TF} \equiv \left[\frac{\left(k_T^{-2} + k_F^{-2}\right)^{1/2}}{k_T^{-3} + k_F^{-3}} \right]^{1/2} \tag{11}$$

where

$$K_T = 120.5\, T^2 \tag{12}$$

$$K_F = 1.54 \times 10^{-6} \frac{E^2}{\phi} \frac{1}{t^2(y)} \tag{13}$$

$$k_T = \frac{\phi(1 - y)}{8.615 \times 10^{-5}\, T} \tag{14}$$

$$k_F = \frac{6.83 \times 10^7 \, \phi^{3/2}}{E} v(y) \tag{15}$$

$$t(y) \cong 1 + \frac{1}{9} y^{5/3} \tag{16}$$

$$v(y) \cong 1 - y^{5/3} \tag{17}$$

$$y \cong \frac{3.79 \times 10^{-4} \, E^{1/2}}{\phi} \tag{18}$$

where

T is the surface temperature (°K)

E is the normal electric field intensity (V/cm)

ϕ is the work function of the surface (electron-volts)

When T is set equal to zero, we obtain the Fowler-Nordheim formula for high-field emission current density. When E is small, Eq. (9) reduces to the Richardson-Schottky formula for electric-field-enhanced thermionic emission current density. Equation (9) is used in the plasmoid ionization buildup equation in Ref. 1 instead of the peak current density formula given there.

Protrusion Heating. The temperature rise of the emitting protrusion is estimated from the results of the analyses of two different emiting situation models. In the first model, it is assumed that the protrusion is in good thermal contact with the bulk of the target material so that both have the same temperature. The temperature of the bulk material surface is then calculated by the heat-conduction model that we have used for vaporization calculations in the low-intensity regime (see Section 2). In the second model, it is assumed that the protrusion is thermally isolated from the bulk of the target material so that the protrusion temperature is determined by its heat capacity and by the absorbed laser radiation. In the parameter regime considered in this model, it can be shown that the electromagnetic skin depth (depth of laser

radiation penetration) is less than the smallest dimension of the assumed protrusion. The protrusion is therefore opaque to the laser radiation. Also, the time for thermal conduction through the protrusion is small compared to the time interval of concern for initiation; hence, the concept of isothermal heating of the entire protrusion volume is applicable. Under these conditions, the temperature T of a protrusion under laser irradiation is given by

$$T = T_o + \frac{\alpha A}{\rho C V} \int_{t=0}^{t} I \, dt \tag{19}$$

where

- T_o is the initial temperature
- α is the effective surface absorptivity over the radiation interception surface area A
- V is the volume
- ρC is the specific volumetric thermal capacity
- I is the laser radiation intensity

The volume of a prolate spheroidal protrusion is

$$V = \frac{2}{3} \pi b^2 h \tag{20}$$

where b is the base radius and h is the height. The interception area presented to incoming radiation at an angle θ_i to the surface normal can be shown to be

$$A = \frac{1}{2} \pi b \left[b \cos \theta_i + \left(h^2 \sin^2 \theta_i + b^2 \cos^2 \theta_i \right)^{1/2} \right] \tag{21}$$

Equations (20) and (21) can be combined to give the area to volume ratio in the form

$$\frac{A}{V} = \frac{3}{4}\frac{1}{h}\left[\cos\theta_i + \left(x^2 \sin^2\theta_i + \cos^2\theta_i\right)^{1/2}\right] \tag{22}$$

where $x \equiv h/b$ is the aspect ratio of the protrustion.

Numerical Results. Calculations of incubation time for prompt initiation of laser-supported absorption waves have been made using temperature-field emission from protrusions whose temperature is calculated from either the conduction or the thermal capacity model.

The quantitative results are illustrated in Fig. 5. The curves labeled "t_c" are the times required to achieve critical electron density in a localized plasmoid above a surface protrusion. This condition is implicitly assumed to be equivalent to initiation of an absorption wave. The calculations were made for an aluminum surface irradiated by a CO_2 laser (10.6-μ wavelength) having the temporal pulse shape of the Battelle laser (Ref. 4). The surface is assumed to possess a prolate spheroidal protrusion of height h ($h = 1$ and $0.5\ \mu$) and of aspect ratio 16. For this geometry, the electric field is intensified by the factor F ($F = 100$) in the neighborhood of the tip of the protrusion. The solid curves (a, b, which overlap) are for no temperature rise (curve a, pure high-field electron emission) and for a temperature rise equal to the bulk material surface-temperature rise calculated by the heat-conduction model that we have used successfully in the LSC wave regime (curve b, thermally augmented high-field electron emission). The dashed t_c curves are for the maximum possible protrusion temperature rise computed under the assumption that heat conduction from the protrusion into the underlying material is negligible. Curves a and b are indistinguishable because the heat-conduction model predicts a very small temperature rise; hence, the thermionic effect is negligible. The solid curve labeled "$t_{1.67}$" is the time required to deliver 1.67 J/cm^2 to the surface, and also represents a good fit to the measured initiation dwell time data from the Battelle experiments (Ref. 4). It can be seen that, although "incubation" dwell times calculated from the thermally augmented field-emission model are not inconsistent with the experimental measurements, the general trend of the experimental data is not well predicted at the lower end of the intensity range.

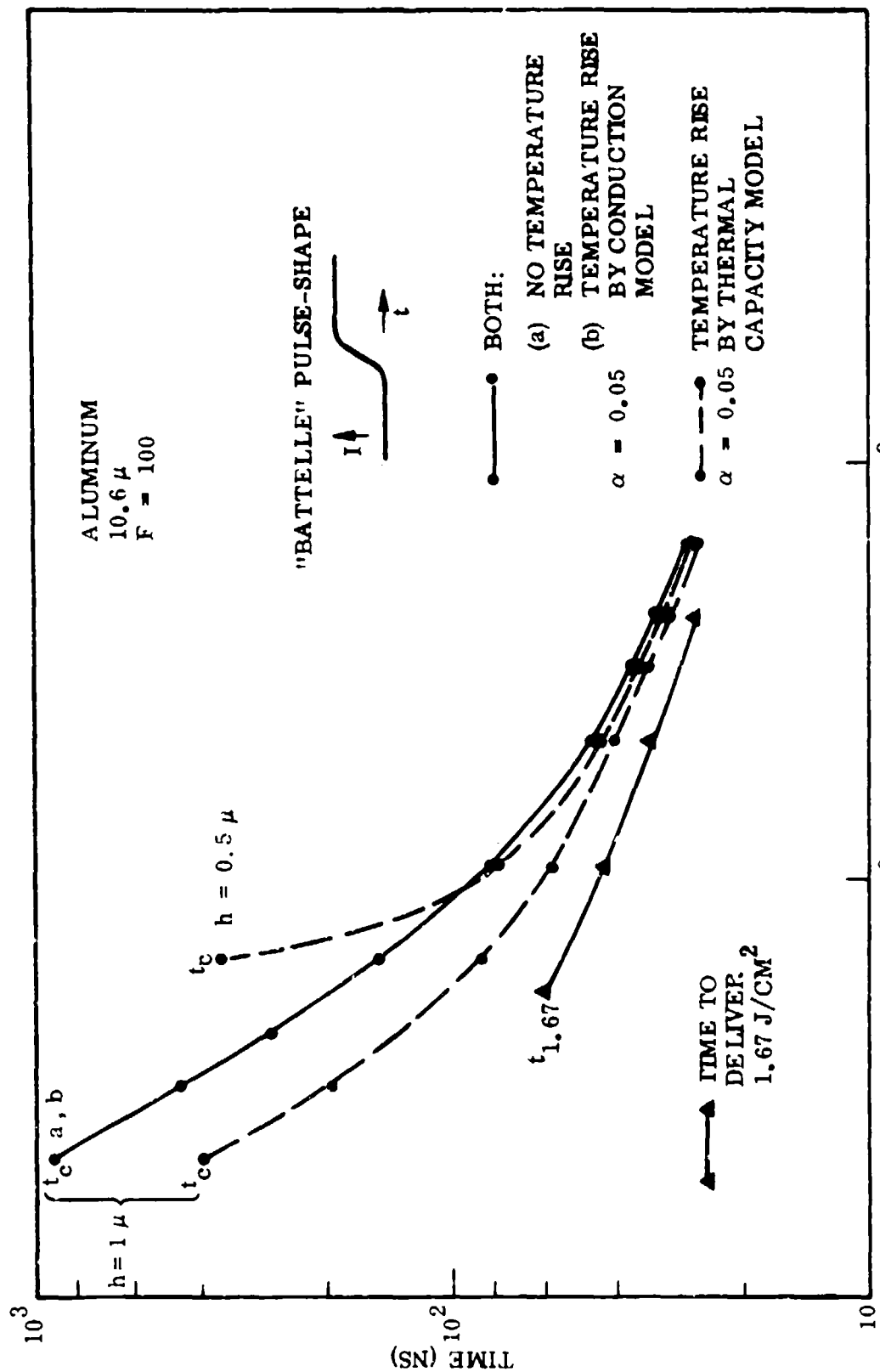

Fig. 5 Incubation Time for Thermally Augmented Field Emission Initiation of Absorption Waves

3.3 THERMIONIC ELECTRON-EMISSION INITIATION MODEL

3.3.1 Model Characteristics

The prompt initiation incubation time measured in the Battelle experiments correlates very well with the time required to deliver a fixed energy density to the target surface (Ref. 4). This agreement suggests that the initiation process might be related to target heating in a thermal capacity mode.

Walters (Ref. 4) examined the plausibility of this argument by making a sequence of calculations and empirical correlations. First, he showed that if thin "lamina" of target material were present on the surface, and were thermally isolated from the bulk of the target material, they could be heated to thermioric-emission temperatures (2000° to 2500°K) in a fraction of the measured initiation delay times if they were thin enough. Second, he showed that under the assumption of steady-state space-charge election distribution, the electron density in the air over the lamina could reach values of the order of 10^{14} electrons/cm^3 for the thermionic electron-emission current densities prevailing under the temperatures previously calculated. Finally, it was inferred that the air breakdown time, for preionized air with the abovementioned "priming" electron density, would also be less than the absorption wave initiation time delay. Thus, Walters found no compelling reason to reject this initiation mechanism.

We have reexamined the purely thermionic electron-emission mechanism in order to formulate a complete, self-consistent model with which to calculate the absorption wave initiation incubation time and to see whether it correlates with experimental data. An analysis of this model for prompt initiation based on thermionic electron-emission from the target surface and concomitant cascade ionization in the ambient atmosphere has been carried out. Figure 6 illustrates the model schematically. It is assumed that thermionic electron-emission takes place from a localized thin surface layer that is thermally isolated from the bulk of the target material and that is heated by absorption of a fraction (α) of the incident laser beam intensity. The emitted electrons act

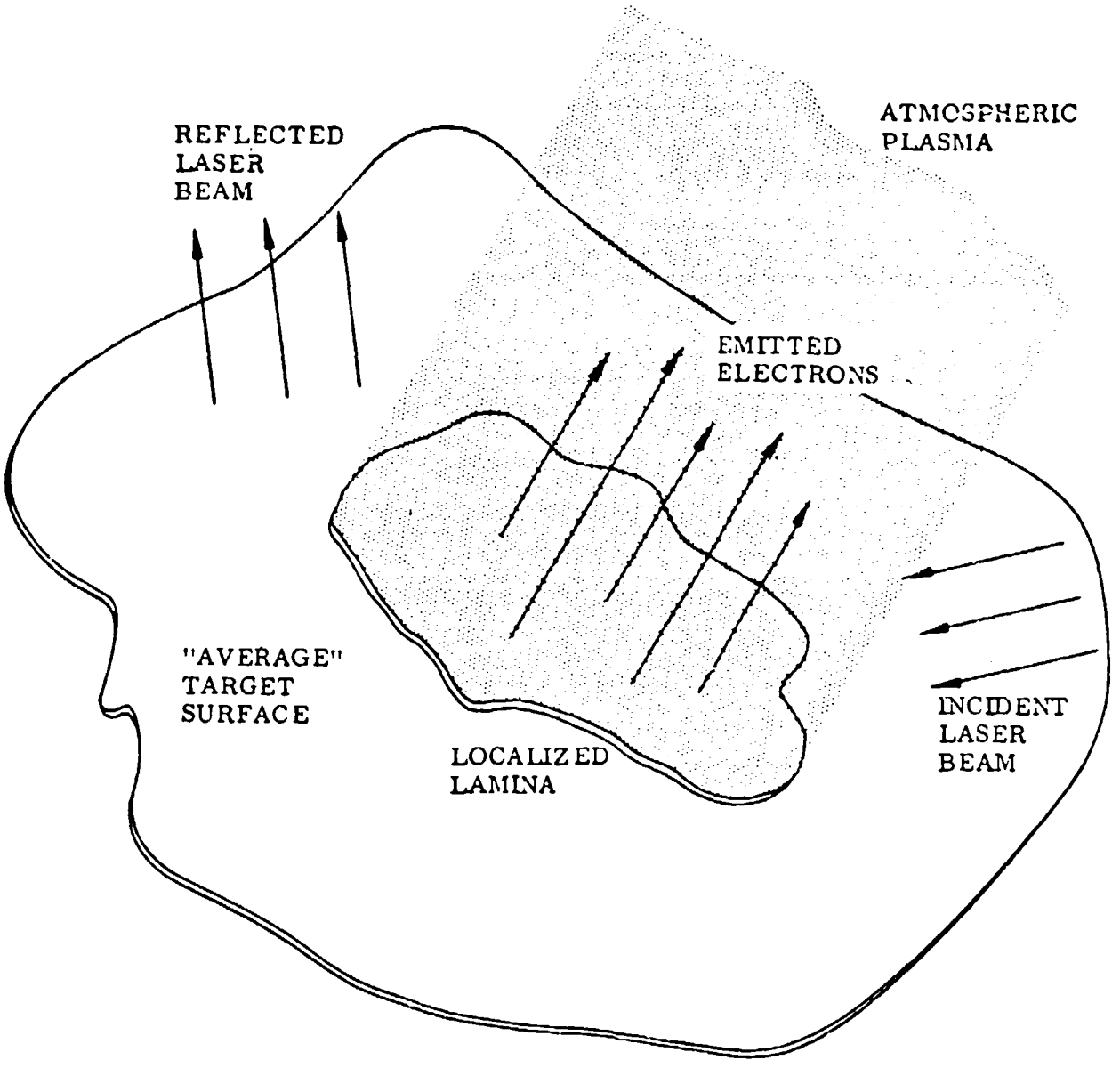

Fig. 6 Localized Plasma Formation Over Surface Lamina

as a "seed" for cascade ionization buildup in the ambient atmospheric region over the emitting area. The absorption wave initiation time was chosen to be that time at which the laser beam intensity at the surface decreased significantly from the incident intensity due to absorption in the plasma layer over the target surface. This corresponds directly to one of the diagnostic measurements used in the Battelle experiments, where "significant" absorption was taken to be a 2-percent decrease in intensity.

3.3.2 Attenuation Through Plasma Layer

The laser beam intensity at the target surface (I_t), which is assumed to be covered by a plasma layer, is calculated by the WKBJ approximation (Ref. 2) to be

$$I_t \cong I_b \exp\left[-\frac{1}{c N_{ec} \cos\theta_i} \int_{z=0}^{\infty} N_e \nu_c \, dz\right] \tag{23}$$

where

I_b	is the incident laser beam intensity
c	is the speed of light
N_{ec}	is the critical electron density for the incident radiation wavelength
θ_i	is the angle of incidence of the beam relative to the surface normal
N_e and ν_c	are the electron density and electron-neutral collision frequency in the plasma layer
z	represents the coordinate dimension normal to the surface

The fractional decrease (D) in intensity at the target due to dissipation in the plasma layer is $(I_b - I_t)/I_b$, which is

$$D = 1 - \exp\left[-\frac{1}{c N_{ec} \cos\theta_i} \int_{z=0}^{\infty} N_e \nu_c \, dz\right] \tag{24}$$

This is the quantity that we must calculate as a function of time as the electron density increases because of both thermionic emission and cascade multiplication.

The power absorbed by the plasma layer, per unit area parallel to the target surface, from the incoming laser beam, is given by $(I_b - I_t) \cos \theta_i$. This can be expressed as $D I_b \cos \theta$. The intensity of the reflected laser beam at the target surface is $(1 - \alpha) I_t$, where α is the surface absorptivity of the emitting area. Beyond the plasma layer, the reflected beam intensity, calculated by the WKBJ approximation, is given by $(1 - \alpha) I_t (1 - D)$. Therefore, the power absorbed by the plasma layer, per unit area parallel to the target surface, from the outgoing reflected laser beam, is given by

$$\left[(1 - \alpha) I_t - (1 - \alpha) I_t (1 - D)\right] \cos \theta_i = (1 - \alpha) I_t D \cos \theta_i$$

Consequently, the total power absorption from both the incident and reflected beams, is given by

$$D I_b \cos \theta_i + (1 - \alpha) I_t D \cos \theta_i$$

which can be written as

$$D I_b \cos \theta_i \left[1 + (1 - \alpha)(1 - D)\right]$$

This power goes into plasma heating (kinetic energy), vibration, dissociation, excitation, ionization, radiation, etc.

3.3.3 Ionization Buildup

In modeling the buildup of electron density in the plasma layer, we have made a number of assumptions such that we overestimate the effectiveness of thermionic initiation. The electron density calculated from the analysis represents an upper bound on the actual electron density that could be achieved. This has the effect of making the incubation time calculated under these assumptions represent a lower bound to the actual time.

Specifically, we assume that all energy absorbed by the plasma layer from the incident and reflected laser beams is effective in producing additional ionization. We neglect the potential effect of space-charge in suppressing the thermionic emission from the surface, and do not consider the loss of electrons by diffusion back to the surface, recombination, attachment to oxygen, etc.

The number of electrons in the plasma layer, per unit area, due to thermionic electron-emission from the surface, is given by

$$Q_E = \int_{t=0}^{t} J_T \, dt \tag{25}$$

where J_T is the thermionic electron emission rate (per unit area). This is just the special case of Eq. (9) for zero normal electric field. Specifically, this is

$$J_T = 7.52 \times 10^{20} \, T^2 \exp\left[- \frac{\phi}{8.615 \times 10^{-5} \, T} \right] \tag{26}$$

where J_T above gives electrons/sec-cm^2; the other quantities have already been defined.

The number of electrons created in the plasma layer, per unit area, due to cascade ionization driven by absorbed laser power, is given by the energy absorbed divided by the energy required to create an ion-electron pair (ϕ_i; ionization potential). This is

$$Q_I = \frac{1}{\phi_i} \int_{t=0}^{t} D I_b \cos \theta_i \left[1 + (1 - \alpha)(1 - D) \right] dt \tag{27}$$

The total number of electrons in the plasma layer, per unit area parallel to the surface at any time (t), is $(Q_E + Q_I)$. We note that

$$Q_E + Q_I = \int_{z=0}^{\infty} N_e \, dz \tag{28}$$

3.3.4 Surface Heating

To calculate the thermionic electron emission it is necessary to know the temperature of the emitting surface. We have approached this calculation from two widely differing viewpoints. One is that there exist on the material surface thin lamina, or "flakes," of target material that are thermally isolated from the underlying bulk material. The other is that heat conduction into the bulk of the target material is rate-limited, so that the temperature rise due to laser power absorption within the skin depth layer at very high incident power densities is affected only by the thermal capacity of the material.

For a thin flake of target material (thicker than the skin depth, however), heating isothermally under laser irradiation, we can use Eq. (19) to give the surface temperature. The area-to-volume ratio is d^{-1}; hence

$$T = T_o + \frac{\alpha \cos \theta_i}{\rho C d} \int_{t=0}^{t} I_t \, dt \tag{29}$$

where d is the thickness of the flake. The effect of oblique incidence is included here through the $\cos \theta_i$ factor.

Under the assumption that heat conduction is severely rate-limited (that is, does not occur at all), the temperature of the surface is given by

$$T = T_o + \frac{2 \alpha \cos \theta_i}{\rho C \delta} \int_{t=0}^{t} I_t \, dt \tag{30}$$

where δ is the electromagnetic skin depth in the material at the laser wavelength. It can be seen that this case is equivalent to the lamina model with $d = \delta/2$. That is, the temperature rise in this case is the same as that calculated for an isothermal flake of thickness equal to one-half the skin depth. The skin depth (δ) is given by (Ref. 14)

$$\delta = \left[\frac{\lambda}{\pi c \mu \sigma}\right]^{1/2} \tag{31}$$

where

λ	is the free-space wavelength
c	is the speed of light
μ and σ	are the inductivity and conductivity of the material

It should be noted that for electrically conductive materials such as metals, a simple classical relationship between the surface absorptivity and the skin depth exists, and can be expressed in the form

$$\frac{\alpha}{\delta} \cong \frac{4\pi}{\lambda} \tag{32}$$

Thus, the ratio α/δ in Eq. (30) is independent of the electrical properties of the material and depends only on the radiation wavelength.

3.3.5 Solution of Equations

The incubation time for prompt initiation of laser-supported absorption waves in the thermionic electron-emission model is taken to be the time at which a significant decrease in laser beam intensity at the target surface occurs. In this context, a "significant" decrease is taken to be a few percent. Provided that we therefore consider values of D in Eq. (24) that are less than one-tenth, we can approximate the exponential term by the first two terms of its power series expansion, giving

$$D \cong \frac{1}{c N_{ec} \cos \theta_i} \int_{z=0}^{\infty} N_e \nu_c \, dz \tag{33}$$

Furthermore, we assume that the electron collision frequency is independent of position in the plasma layer, so that it can be removed from the integral. Then, using Eq. (28) gives

$$D \cong \frac{\nu_c}{c N_{ec} \cos \theta_i} (Q_E + Q_I) \tag{34}$$

Again, using the condition that we seek a solution only for small values of D, Eq. (27) can be approximated by

$$Q_I \cong \frac{(2 - \alpha) \cos \theta_i}{\phi_i} \int_{t=0}^{t} D I_b \, dt \tag{35}$$

Using Eqs. (25) and (35) in Eq. (34) gives

$$D \cong \frac{\nu_c}{c N_{ec} \cos \theta_i} \left[\int_{t=0}^{t} J_T \, dt + \frac{(2 - \alpha) \cos \theta_i}{\phi_i} \int_{t=0}^{t} D I_b \, dt \right] \tag{36}$$

Differentiating this equation with respect to t, and rearranging, gives

$$\frac{dD}{dt} - \frac{\nu_c (2 - \alpha)}{c N_{ec} \phi_i} I_b D \cong \frac{\nu_c}{c N_{ec} \cos \theta_i} J_T \tag{37}$$

This differential equation can be solved to give

$$D \cong \exp\left[\int_{t=0}^{t} \frac{\nu_c (2-\alpha)}{c\, N_{ec}\, \phi_i} I_b\, dt\right] \cdot \int_{t=0}^{t} \frac{\nu_c}{c\, N_{ec} \cos\theta_i} J_T \exp\left[-\int_{t=0}^{t} \frac{\nu_c (2-\alpha)}{c\, N_{ec}\, \phi_i} I_b\, dt\right] dt \tag{38}$$

If we assume that ν_c is substantially independent of time during most of the ionization buildup, it can be removed from under the integral. The energy density delivered by the laser beam up to any given time [E(t)] is given by

$$E(t) = \int_{t=0}^{t} I_b\, dt \tag{39}$$

Thus, Eq. (38) can be written

$$D \cong \exp\left[\frac{\nu_c (2-\alpha)}{c\, N_{ec}\, \phi_i} E(t)\right] \cdot \int_{t=0}^{t} \frac{\nu_c}{c\, N_{ec} \cos\theta_i} J_T \exp\left[-\frac{\nu_c (2-\alpha)}{c\, N_{ec}\, \phi_i} E(t)\right] dt \tag{40}$$

For small values of D, the integral of I_t in the heating calculations of Eqs. (29) and (30) can be approximated by the integral of I_b; hence

$$\int_{t=0}^{t} I_t\, dt \cong E(t) \tag{41}$$

which is used in the calculation of J_T. This now gives the variation of D with time explicitly.

In the Battelle experimental work, absorption wave initiation time was measured as the time at which the laser beam intensity at the target surface (observed through a hole in the target) decreased significantly (approximately 2 percent) from the incident beam intensity, because of absorption by the plasma layer over the target.

Therefore, in our analysis, we ask: "At what time (t_a) does D become significant (say, two percent)?" This then gives an implicit equation for t_a in the form

$$\frac{\nu_c}{c\, N_{ec} \cos\theta_i} \exp\left[\frac{\nu_c (2-\alpha)}{c\, N_{ec}\, \phi_i} E(t_a)\right] \cdot \int_{t=0}^{t=t_a} J_T \exp\left[-\frac{\nu_c (2-\alpha)}{c\, N_{ec}\, \phi_i} E(t)\right] dt = 0.02 \tag{42}$$

It can be seen that the solution does indeed depend on the energy density delivered by the laser beam, but not in a very simple way. Equation (42) is solved numerically to get values of t_a for specified input parameters and laser pulse shapes.

3.3.6 Numerical Results

Figure 7 shows the results of some specific solutions of Eq. (42) for an aluminum target irradiated by CO_2 lasers (10.6-μ wavelength) having temporal pulse shapes characteristic of either the Battelle or Boeing laser outputs. The Battelle laser pulse intensity history was modeled as an 8-ns delay during which the intensity is negligible, followed by a 37-ns linear increase in intensity up to the peak intensity value. The Boeing laser pulse intensity history was modeled as a 1.39-μsec linear increase in intensity up to the peak intensity value.

In these calculations we have assumed normal incidence of the laser beam ($\theta_i = 0$), an effective air ionization potential (ϕ_i) of 15 electron-volts, an effective surface absorptivity of five percent ($\alpha = 0.05$), an initial surface temperature (T_o) of 300°K, and an effective surface work function (ϕ) of 3.74 electron-volts. The critical electron density (N_{ec}) for 10.6-μ wavelength radiation is 1.1×10^{19} electrons/cm^3, and the specific volumetric thermal capacity (ρC) of aluminum is 2.35 J/cm^3 - °K. The electron collision frequency (ν_c) in the ambient air, at one atmosphere pressure, was calculated for an electron temperature of 2 electron-volts ($\nu_c = 7 \times 10^{11}$ sec^{-1}). The "free" parameter in these calculations is the layer thickness (d), for the lamina model. The minimum value of d is constrained to be greater than the electromagnetic skin depth (δ) of the material, in order for the layer to absorb the fraction α of the incident laser beam intensity. Thus, the curves labeled $d = \delta$ represent the physically realistic minimum values for t_a for a thermally isolated flake. The other curves show the effect of thickening the layer. Also shown in Fig. 7 is the time required to deliver 1.67 J/cm^2 for each of the two pulse shapes. As noted earlier, this curve represents well the experimentally measured absorption wave formation time (time for 2-percent intensity reduction) in the Battelle experiments (Ref. 4). No formation time measurements were made in the Boeing experiments. It can be seen, then, that this thermionic emission model, with suitably chosen parameters, can lead to calculated absorption wave formation times that agree quite well with available (Battelle) experimental data.

For the rate-limited heat conduction model, the results would be very similar to those obtained above, except that there is no "free" parameter. The calculated initiation time would be the same as a $d = \delta/2$ curve. That is, the predictions for t_a for the rate-limited heat conduction model would lie just below the lowest curve (the $d = \delta$ curve) shown on Fig. 7 for each of the two pulse shapes. Therefore, this model is not inconsistent with the experimental results when one considers that the predicted t_a values represent lower limits to the initiation dwell time.

The actual time required for prompt initiation of laser-supported absorption waves via the thermionic electron-emission mechanism will be greater than the t_a values given by Eq. (42) for several reasons. Formation of a space-charge layer over the emitting

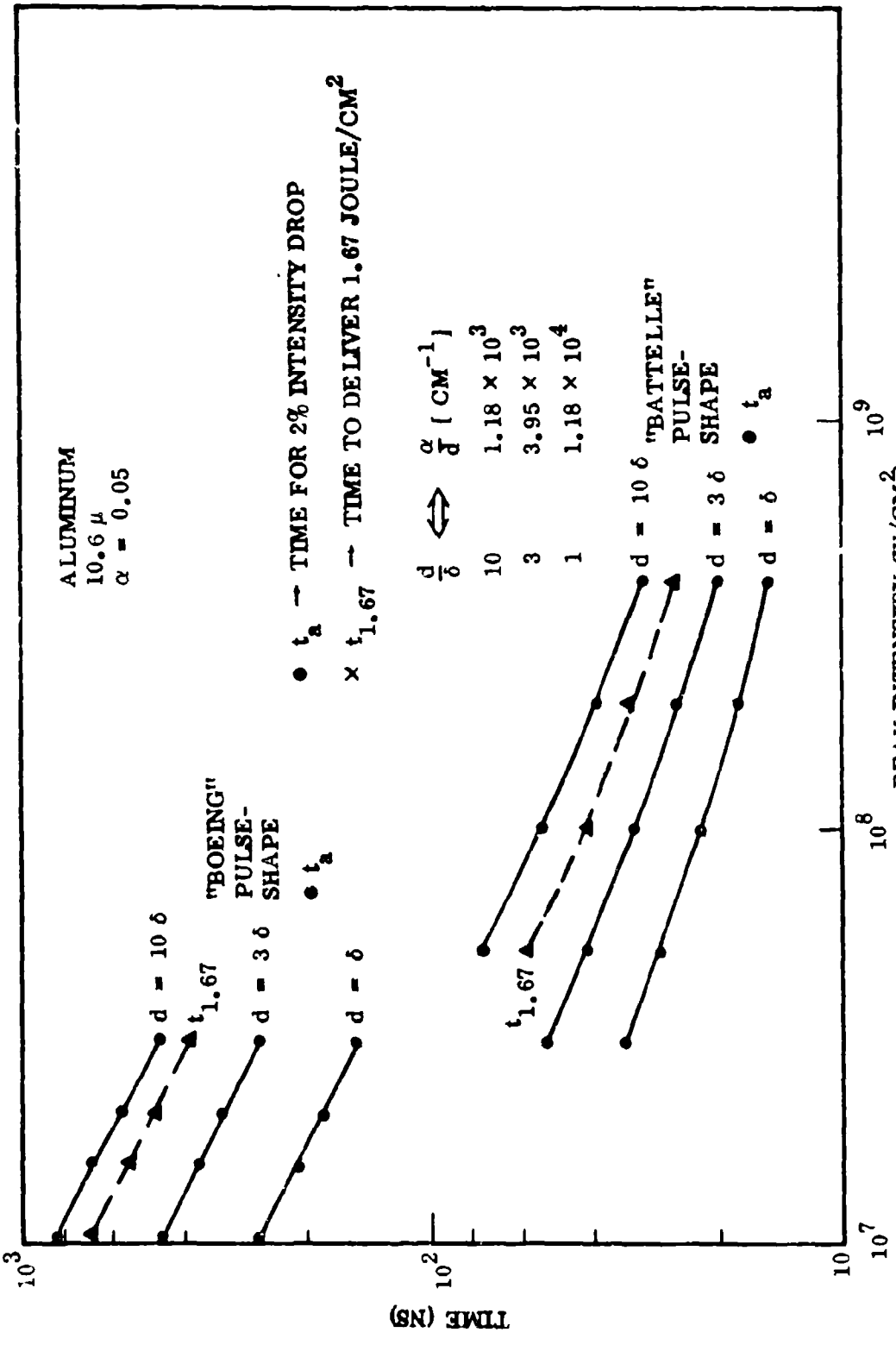

Fig. 7 Incubation Time For Thermionic Emission Initiation of Absorption Waves

surface will suppress the electron emission. Loss of electrons by diffusion, recombination, and attachment will slow down the free-electron density rate of increase. Electron energy loss to processes other than ionization, such as kinetic energy, vibrational and electronic excitation, dissociation, and radiation, will also depress the rate of increase of free electrons. Also, the effective collisional coupling between free electrons and vibrational modes in air may tend to keep the electron temperature from rising as high as assumed in the calculations presented here. This would make the electron collision frequency smaller. This would, in turn, decrease the rate of energy absorption from the laser beam and consequently slow down the ionization cascade. In the rate-limited thermal conduction model, the temperature rise of the surface should actually start out the same as in the bulk conduction model during the initial low-intensity part of the laser pulse risetime, and then later at higher intensity become predominantly heat-capacity-controlled. This would lengthen the time required for the surface to reach the temperature at which thermionic emission could begin and trigger the ionization cascade.

3.4 CONCLUSIONS AND RECOMMENDATIONS

We have investigated two mechanisms that could be responsible for prompt initiation of laser-supported absorption waves in air at beam intensities above 10 MW/cm^2. These are high-field electron-emission from protrusions on the target surface, and thermionic electron-emission from anomalous patches on the target surface. Either of these processes potentially could be responsible for the production of triggering electrons that start an ionization cascade in the air over the surface under laser irradiation. These localized "breakdown" regions then develop into traveling absorption waves. As a result of our analyses of models of these two initiation mechanisms, we have been able to show that neither one should be eliminated from consideration until further experimental evidence is available. In fact, it is likely that both high-field and thermionic mechanisms play some role in the initiation processes, with one mechanism dominant over the other alternately at the two extremes of the laser beam intensity range involved.

The high-field mechanism was favored initially because there is no thermal time-lag involved in the start of electron emission from the target surface. That this held promise for extremely rapid initiation of absorption waves was indicated by experimental data.

Although calculations of prompt absorption wave incubation time based on the thermally augmented high-field electron-emission model are not inconsistent with the experimental measurements, the general trend of the experimental data is not well predicted at the lower end of the intensity range. It should be pointed out, however, that near this threshold the numerical results of this model will be very sensitive to the detailed temporal behavior of the laser pulse intensity.

The thermionic mechanism was reexamined in detail after experimental data became available that showed that initiation time could be correlated with time to deliver a constant energy density to the target, because this observed behavior suggested a heat-capacity effect. Calculations of prompt absorption wave incubation time based on the thermionic electron-emission model, with suitably chosen parameters, agree quite well with available experimental data. Either of two widely differing assumptions about the detailed behavior of the intensely irradiated target surface can lead to the aforementioned predictions of the thermionically emitted electrons that induce the ionization cascade. One is the presence of surface lamina, or flakes, that are thermally isolated from the underlying material, and that are of the order of the electromagnetic skin depth in thickness. This has been explicitly postulated in the calculations made thus far. The other assumption is that heat conduction into the bulk of the target material is rate-limited, so that the temperature rise due to laser power absorption within the skin depth layer at very high incident power densities is affected only by the thermal capacity of the material. Classical heat transfer theory, based on nonsaturating (or non-rate-limited) thermal conduction, predicts a transition from conduction-limited to heat-capacity-limited temperature rise behavior at much higher intensities than we have considered here. The possibility that such a transition could occur at lower intensity due to nonlinear phenomena has far-reaching fundamental implications.

Each of the initiation mechanisms examined in our theoretical study requires the acceptance of some important assumptions about the characteristics of the target. For the pure high-field electron-emission mechanism, there must be large, very pointed protrusions on the surface that enhance the normal electric field intensity by a factor of order 100. For thermally enhanced high-field electron-emission, these protrusions must be

thermally isolated from the bulk of the target material. For pure thermionic electron-emission, very thin flakes of target material that are thermally isolated from the underlying target material must be present. These are all surface characteristics of the target. The rate-limited heat-transfer assumption, used in a thermionic electron-emission model, is more fundamental. However, such behavior need not be an intrinsic characteristic of the target material, but rather the result of subsurface lattice (crystal) structure defects. The applicability of any of these assumptions must be clarified by detailed target preparation and/or examination in all future experimentation.

We suggest that additional experimental evidence be gathered to provide the basis for the selection of the dominant initiation mechanism under various circumstances. Some detailed recommendations for such experimental work have already been given (Ref. 2).

A critical difference between the high-field and thermionic emission mechanisms is the kinetic energy of the emitted electrons. If high-field emission is active, the emitted electrons will be accelerated to energies of the order of 10 electron-volts and above. On the other hand, thermionic emission will produce emitted electrons with average energies well below one electron-volt. Thus, measurement of the energy distribution of emitted electrons (in a vacuum) should easily differentiate between the two mechanisms.

The time history of the emission current, relative to the time history of laser beam intensity, will also help differentiate between the two mechanisms. As pointed out earlier, high-field electron-emission essentially follows the instantaneous radiation intensity, while thermionic electron-emission suffers a time-lag due to the temperature response of the target.

Both emission mechanisms display a sensitivity to the angle of incidence of the laser radiation. As the incident laser beam approaches grazing incidence, the temperature rise of the surface will become slower, thus delaying thermionic emission.

In all experiments involved in gathering evidence to elucidate the nature of the electron-emission from the target surface, detailed surface conditions and configurations should be determined. The spatial resolution scale must be less than 1 μ (for 10.6-μm radiation experiments); this determination indicates the extensive use of scanning electron beam microscopy. More extensive samplings of target materials and surface configurations than have been available to date are also needed.

Section 4

EFFECT OF RADIAL FLOW ON THE SPEED OF AN AXISYMMETRIC SUBSONIC LSC WAVE

In the Midterm Term Technical Report (Ref. 1), an analysis of the axisymmetric, subsonic Laser-Supported Combustion (LSC) wave, freely propagating through air along a finite-diameter laser beam was made. A complete set of integral equations which govern the two-dimensional wave motion was derived based on a generalized integral method. Results were presented for a case in which the radial gas motion was neglected, but which included radial transport of thermal radiation and heat conduction. This result represents the solution to the energy conservation equation when the latter is decoupled from the radial momentum equation by the assumptions of zero radial flow ($\rho v = o$) and constant axial mass flow ($\rho u = \rho_o u_o$). The calculated wave speed is therefore that of a quasi-one-dimensional wave and is about a factor of three lower than the experimental value.

To obtain a fully coupled two-dimensional wave solution, the set of integral equations presented in Ref. 1 has to be solved simultaneously. To do so, we have followed a somewhat complicated iteration scheme which was described in detail in Ref. 1. Unfortunately, this multilevel iteration is very unstable, especially in the radial flow ($F_{2,0}$) iteration. Various stabilization methods were tried, but without much success.

In an attempt to solve the radial flow field ($F_{2,0}$) and the axial flow field ($F_{1,0}$) without the iteration on $F_{2,0}$, we have converted the integral form of the η-integrated continuity and momentum equation back into the differential form. They can be written as

$$\delta = C \left(1 - F_{1,0}\right)^{1/6} \tag{43}$$

$$\frac{d F_{1,0}}{dx} + \frac{2 F_{2,0}}{\delta} = 0 \tag{44}$$

$$\frac{d F_{2,0}}{dx} = \frac{A_1 Y - A_2 F_{2,0}^2 - A_3 F_{2,0}}{42 F_{1,0} F_{5,0} + 13 (F_{1,0} + F_{2,0}) + 12} \tag{45}$$

$$\frac{dY}{dx} = A_4 F_{2,0} - A_5 \tag{46}$$

$$F_{3,0} = 1 + \frac{\gamma M^2}{\left(1 - F_{1,0}\right)^{1/12}} Y$$

where

$$C = \text{a constant, } A_1 = \frac{180}{C \left(1 - F_{1,0}\right)^{1/4}}$$

$$A_2 = \frac{63 - 4.7 F_{5,0} + \frac{1}{3 (1 - F_{1,0})} \left[16 F_{1,0} F_{5,0} - 11 (F_{5,0} + F_{1,0}) - 54\right]}{C \left(1 - F_{1,0}\right)^{1/6}}$$

$$A_3 = (42 F_{1,0} + 13) \frac{d F_{5,0}}{dx}$$

$$A_4 = \frac{1}{C \left(1 - F_{1,0}\right)^{1/12}} \left[\frac{520 F_{1,0} F_{5,0} + 86 (F_{5,0} + F_{1,0}) + 85}{126} + \frac{1}{42 (1 - F_{1,0})} \left(8 F_{1,0}^2 F_{5,0} - F_{5,0} - 2 F_{1,0} - 5\right)\right]$$

$$F_S = \frac{48 F_{1,0}^2 + 12 F_{1,0} + 3}{63} \left(1 - F_{1,0}\right)^{1/12} \frac{d F_{5,0}}{dx}$$

Equations (43) and (44) are the first two η-moments of the continuity equations and Eqs. (45) and (46) are, respectively, the first moments of the radial and axial momentum equations. The details of these η-moments and the definitions of symbols were described in Ref. 1. For a given $F_{5,0}(X)$ and wave speed, Eqs. (44) to (46) can be integrated from wavefront ($X = -1$) provided that the initial slopes $\frac{dF_{2,0}}{dx}$, $\frac{dY}{dx}$, $\frac{dF_{1,0}}{dx}$ and the constant C can be determined.

The equations are singular at the wavefront because of the following boundary conditions: $F_{1,0} = 1$. $F_{5,0} = 1$, $F_{2,0} = 0$, at $X = -1$. On the basis of physical argument, it can be shown that $\frac{dF_{5,0}}{dx}$ must be finite at $X = -1$. A local solution to Eq. (45) then can be found near the wavefront. This solution has the following form

$$F_{2,0} \sim b(1 - F_{1,0})^{1/8} \tag{47}$$

Using Eq. (47), the initial slope of $F_{1,0}$, Y and $F_{2,0}$ can be determined within a multiplicative constant b. This constant and the constant c are to be determined by the two downstream boundary conditions, $F_{2,0} = 0$ and $Y = 0$ at $X \to \infty$. This solution scheme relieves us from iteration on $F_{2,0}$, but we need to iterate on the two constants b and c. In fact, iterations cannot be avoided because of the split boundary conditions of the governing equations. In view of the extreme instability of the integral iteration (on $F_{2,0}$) mentioned above, this new scheme seems to provide a viable alternative. However, the limited scope of the present study did not allow modification of the computer code to obtain detailed numerical solutions with this new scheme.

Thus, we have not been successful in obtaining a complete two-dimensional LSC wave solution that includes the effect of radial flow. However, a sufficient set of trial calculations were made with the original integral iteration scheme to show that the axial mass flow, normalized by the free-stream mass flow, is always less than unity within the wave. Hence, in the two-dimensional case, the total mass flow that is heated upon entering the wave is always less than that predicted by the purely one-dimensional model. This means that the radial flow always tends to increase the wave speed over that predicted by the purely one-dimensional model. In the following paragraphs, we estimate quantitatively the magnitude of this effect.

Two papers dealing with the one-dimensional LSC wave appeared recently (Refs. 15 and 16). Aside from their differences in treating the radiative transport, they also differ in treating the radial energy loss due to heat conduction. In Ref. 15, radial conductive loss is neglected altogether; in Ref 16, on the other hand, it is assumed

linearly proportional to temperature. We shall first demonstrate that the energy equation employed in Ref. 15 corresponds to the η-integrated axisymmetric energy equation, while the energy equation employed in Ref. 16 corresponds to the axisymmetric energy equation evaluated at the axis of symmetry. We shall then estimate the effect of radial flow in these two cases separately.

The axisymmetric energy equation in dimensional form is (Ref. 1)

$$\rho u \frac{\partial h}{\partial x} + \rho v \frac{\partial h}{\partial r} = \frac{\partial}{\partial x}\left(\frac{\kappa}{c_p}\frac{\partial h}{\partial x}\right) + \frac{1}{r}\frac{\partial}{\partial r}\left(r \frac{k}{c_p}\frac{\partial h}{\partial r}\right) + K_\nu S H (r - R_o) + \nabla \cdot \vec{Q} \qquad (48)$$

After multiplying Eq. (48) by r, integrating it from 0 to ∞, employing the continuity equation, and assuming that $r \frac{\partial h}{\partial r}\Big)_{r \to \infty} = 0$, $r\rho v)_{r \to \infty} = 0$, $\frac{k}{c_p}$ = constant, we obtain

$$\frac{\partial}{\partial x}\left[\overline{\rho u}\int_0^\infty r\, h\, dr\right] = \frac{\partial}{\partial x}\left[\frac{k}{c_p}\frac{\partial \int_0^\infty r\, h\, dr}{\partial x}\right] + \int_0^\infty K_\nu S H (r - R_o)\, r\, dr + \int_0^\infty r \nabla \cdot \vec{Q}\, dr \qquad (49)$$

where

$$\overline{\rho u} = \frac{\int_0^\infty \rho u\, r\, h\, dr}{\int_0^\infty r\, h\, dr}$$

In the one-dimensional model, $\overline{\rho u} = \rho_o u_o$ = constant. In the axisymmetric case, there is another uniform state that corresponds to the location where the final temperature is reached far behind the wavefront and where $\overline{\rho u} = (\overline{\rho u})_\infty$ = constant. This latter constant represents the mass flow that enters the high-temperature core and is the dominant parameter that influences the wave speed. For estimating the radial flow effect on the wave speed, we assume

$$\frac{\partial}{\partial x}\left[\overline{\rho u}\int_0^\infty r\,h\,dr\right] \simeq (\overline{\rho u})_\infty \frac{\partial}{\partial x}\int_0^\infty r\,h\,dr \tag{50}$$

where $(\overline{\rho u})_\infty$ denotes the average mass flow at $T = T_\infty$ $(X \to \infty)$. Hence, if we write

$$\overline{h} = \int_0^\infty r\,h\,dr,\quad \overline{T} = \int_0^\infty r\,\frac{h}{c_p}\,dr$$

$$K\,S = \int_0^\infty r\,K_\nu\,S\,H\,(r - R_o)\,d\,r \quad \text{and} \quad \phi = -\int_0^\infty r\nabla\cdot\vec{Q}\,dr$$

Equation (49) is then identical to that treated in Ref. 15. Therefore,

$$u_o\ (\text{radial flow included}) = \left[\frac{\rho_o\,u_o}{(\overline{\rho u})_\infty}\right]u_o\ (\text{one-dimensional}) \tag{51}$$

In order to determine $(\overline{\rho u})_\infty$, the following simplifications are made:

(1) The wave shape functions δ is assumed to be a constant δ_∞. It can be shown from Eq. (43) that the variation of δ is slow except near the wave front; therefore, the assumption $\delta \approx \delta_\infty$ = constant far behind the front is reasonable.

(2) The functional relationship between the pressure field and the axial flow momentum is given by the one-dimensional axial momentum equation.

(3) ρv is assumed to be small so that it is neglected in the radial momentum equation.

Under these approximations, the continuity and momentum equations in dimensional form are

$$\frac{\partial \rho u}{\partial x} + \frac{1}{\delta_\infty \eta}\frac{\partial}{\partial \eta}(\eta \rho v) = 0 \tag{52}$$

$$\rho u^2 + p = \rho_o u_o^2 + p_o \tag{53}$$

$$\rho u \frac{\partial v}{\partial x} = \frac{1}{\delta_\infty} \frac{\partial p}{\partial \eta} \tag{54}$$

where $\eta = \frac{r}{\delta_\infty}$

By combining Eqs. (53) and (54), we obtain

$$\frac{\partial v}{\partial x} = \frac{1}{\delta_\infty}\left[\frac{1}{\rho} \frac{\partial \rho u}{\partial \eta} + \frac{\partial u}{\partial \eta}\right] \tag{55}$$

Equations (52) and (55) are to be solved for ρu and ρv as functions of ρ, subject to the following boundary conditions: at $x \to -\infty$, $\rho u = \rho_o u_o$, $\rho v = 0$; at $x \to \infty$, $v = 0$, $\frac{dv}{dx} = 0$, $\frac{du}{dx} = 0$.

As outlined in Ref. 1, we assume the radial profiles

$$\rho u = \rho_o u_o \left(F_{1,0} + (1 - F_{1,0})\,\eta^2\right) \qquad \rho v = \rho_o u_o\, \eta\,(1 - 1/3\,\eta^2)\, F_{2,0}$$

$$h = h_o \left(F_{4,0} + (1 - F_{4,0})\,\eta^2\right) \qquad \frac{1}{\rho} = \frac{1}{\rho_o}\left(F_{5,0} + (1 - F_{5,0})\,\eta^2\right)$$

(56)

Based on the profiles, we approximate $\overline{\rho u}$ as

$$\overline{\rho u} \cong \frac{\int_0^1 \eta\, \rho\, u\, h\, d\eta}{\int_0^1 \eta\, h\, d\eta} = \frac{2/3\left[F_{1,0} F_{4,0} + 1/2\,(F_{1,0} + F_{4,0}) + 1\right] \rho_o u_o}{1 + F_{4,0}}$$

Since $F_{4,0}$ represents the dimensionless enthalpy at the line of symmetry, it is directly proportional to the temperature. From the one-dimensional solution, we have $T_\infty >> T_o$. Therefore, $\left(F_{4,0}\right)_\infty >> 1$, and we obtain

$$(\overline{\rho u})_\infty \simeq 2/3\left[\left(F_{1,0}\right)_\infty + 1/2\right]\rho_o u_o \tag{57}$$

where $\left(F_{1,0}\right)_\infty$ denotes $F_{1,0}$ at $x \to \infty$

We note that at $x \to \infty$, $v \to 0$, and $\frac{dv}{dx} \to 0$ for all η; hence, to find $\left(F_{1,0}\right)_\infty$, it is only necessary to set the η-moment of the right-hand side of Eq. (55) to zero, i.e.,

$$\int_0^1 \eta\left[\frac{1}{\rho}\frac{\partial \rho u}{\partial \eta} + \frac{\partial u}{\partial \eta}\right]_{x\to\infty} d\eta = 0$$

Thus, we obtain

$$\left(F_{1,0}\right)_\infty = \frac{\left(F_{5,0}\right)_\infty + 9}{6\left(F_{5,0}\right)_\infty + 4}$$

Upon assuming a perfect gas equation of state, we have $F_{5,0} \sim F_{4,0}$; hence, $\left(F_{5,0}\right)_\infty >> 1$, so that

$$\left(F_{1,0}\right)_\infty \simeq 1/6 \tag{58}$$

Upon substituting (58) into (57), we find $\frac{\rho_o u_o}{(\overline{\rho u})_\infty} = \frac{9}{4}$. The effect of radial flow in this case is therefore to increase the wave speed as given in Ref. 15 by a factor of 9/4. Comparisons between wave speeds are shown in Fig. 8.

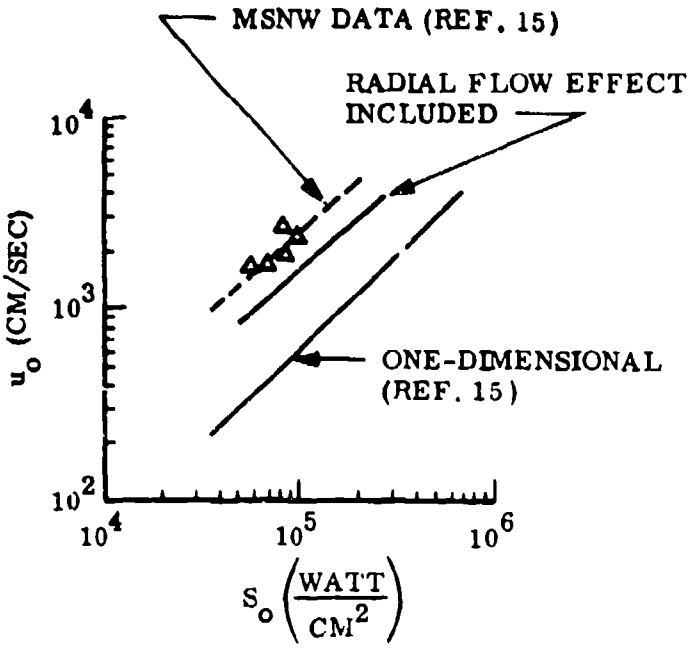

Fig. 8 Propagation Velocity Versus Laser Flux Corresponding to a CO_2 Laser

It is of interest to obtain an approximate solution for the axial mass flow $F_{1,0}$ and the r-derivative of the radial flow $F_{2,0}$ on the line of symmetry. This solution will demonstrate the significant difference between the one- and two-dimensional cases.

After substituting Eq. (56) into Eqs. (52) and (55), multiplying the resulting equation by η, and then integrating them from $\eta = 0$ to $\eta = 1$, we obtain the governing equations for $F_{1,0}$ and $F_{2,0}$ as

$$\frac{d F_{1,0}}{dx} = -\frac{8}{3\delta_\infty} F_{2,0} \tag{59}$$

$$\frac{d}{dx}\left[F_{2,0}\,(8 + 6\,F_{5,0})\right] = \frac{7}{\delta_\infty}\left[F_{5,0} + 9 - F_{1,0}\,(6\,F_{5,0} + 4)\right] \tag{60}$$

The typical one-dimensional solution for temperature is shown in Fig. 9.

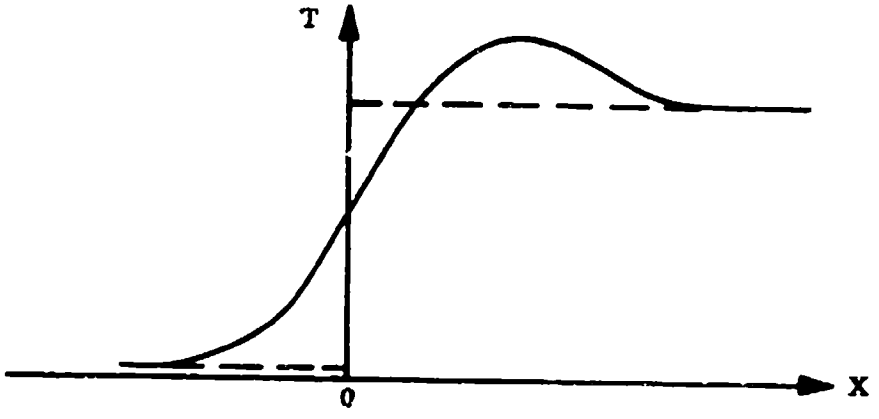

Fig. 9 One-dimensional Subsonic LSC Wave Temperature Profile

To obtain an analytic solution to Eqs. (59) and (60) , the temperature profile is assumed to be approximated by the dotted line as shown in Fig. 9. Now, for constant pressure, $F_{5,0} \sim T$, we therefore assume

$$\begin{aligned} F_{5,0} &= 1 && x < 0 \\ F_{5,0} &= \left(F_{5,0}\right)_\infty >> 1 && x > 0 \end{aligned} \tag{61}$$

Under this assumption and the conditions that, at $x \to -\infty, F_{1,0} = 1$, $\frac{dF_{1,0}}{dx} = 0$, at $x \to \infty$ $\frac{dF_{1,0}}{dx} = 0$, at $x = 0$ $F_{1,0}(0^+) = F_{1,0}(0^-)$ and $\frac{dF_{1,0}(0^+)}{dx} = \frac{dF_{1,0}(0^-)}{dx}$, we obtain the following solutions for $F_{1,0}$ and $F_{2,0}$

$$F_{1,0} = 1 - 0.452\, e^{\frac{1}{\delta_\infty}\sqrt{\frac{40}{3}}x} \qquad x < 0$$

$$= 0.382\, e^{-\frac{1}{\delta_\infty}\sqrt{\frac{56}{3}}x} + 1/6 \qquad x > 0$$

$$F_{2,0} = 0.619\, e^{\frac{1}{\delta_\infty}\sqrt{\frac{40}{3}}x} \qquad x < 0$$

$$= 0.619\, e^{-\frac{1}{\delta_\infty}\sqrt{\frac{56}{3}}x} \qquad x > 0$$

These solutions are plotted in Fig. 10 for $\delta_\infty = 1$; we see that the axial mass flow is substantially reduced due to radial flow.

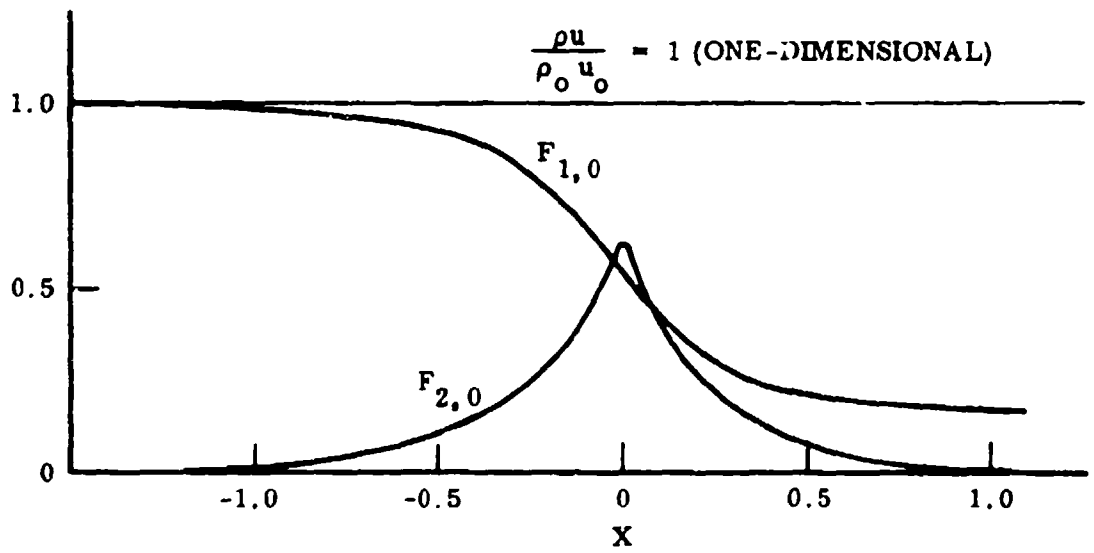

Fig. 10 Axial Mass Flow ($F_{1,0}$) and r-Derivative of Radial Flow ($F_{2,0}$) on the Line of Symmetry

We now examine the behavior at the line of symmetry, where $\rho v = 0$. Equation (48) reduces to

$$\rho u \frac{\partial h}{\partial x} = \frac{\partial}{\partial x}\left(k \frac{\partial T}{\partial x}\right) + 2 \frac{k}{c_p} \frac{\partial^2 h}{\partial r^2}(0) + \frac{ds}{dx} + \frac{dQ}{dx} \tag{62}$$

If we write $\rho u = (\rho u)_\infty$ = constant, $2 \frac{k}{c_p} \frac{\partial^2 h}{\partial \eta^2}(0) = -j_c$, $S = \phi$ and $Q = -F_r$, Eq. (62) becomes identical to that treated in Ref. 16. The wave speed which includes the radial flow effect is again given by Eq. (51).

In this case $(\rho u)_\infty$ is to be determined by setting the right-hand side of Eq. (55) to zero at line of symmetry, i.e.,

$$\frac{1}{\delta_\infty}\left[\frac{1}{\rho} \frac{\partial \rho u}{\partial \eta} + \frac{\partial u}{\partial \eta}\right]_{\eta = 0,\, x \to \infty} = 0 \tag{63}$$

Because of the ellipticity of the governing equations, profiles in η are required even though only the line of symmetry solution is sought. We again assume the profile given by Eq. (56). From (56) and (62) we obtain

$$(\rho u)_\infty = \rho_o u_o \left(F_{1,0}\right)_\infty = \rho_o u_o \left[\frac{2\left(F_{5,0}\right)_\infty}{3\left(F_{5,0}\right)_\infty - 1}\right]$$

Again, since $F_{5,0\,\infty} \gg 1$, we have

$$\frac{\rho_o u_o}{(\rho u)_\infty} = \frac{3}{2} \tag{64}$$

The one-dimensional wave speed given in Ref. 15 is to be increased by a factor of 3/2 in order to account for the radial flow effect. Comparisons between wavespeeds are listed in Table 1 for those cases treated numerically in Ref. 13.

Table 1

COMPARISONS OF THE TWO-DIMENSIONAL WAVESPEED WITH THE RESULTS FROM THE ONE-DIMENSIONAL MODEL OF REF. 16

	u_o		
	Case 1	Case 2	Case 3
One-dimensional, linear theory (Ref. 16)	9.36	62.5	35.75
Radial effect included [Eq. (64)]	14	94.4	50.6
Ref. 16	40	75	57

In conclusion, from the comparisons shown in Fig. 8 and Table 1, we see that the omission of radial flow in the one-dimensional LSC wave model may be largely responsible for the sizable discrepancy between the one-dimensional results and experimentally measured wavespeeds.

Section 5
REFERENCES

1. P. D. Thomas, H. M. Musal, and Y. S. Chou, Laser Beam Interaction – Part II, Midterm Technical Report, LMSC-D401354, Lockheed Palo Alto Research Laboratory, Palo Alto, California, Apr 1974

2. P. D. Thomas and H. M. Musal, A Theoretical Study in Laser-Target Interaction, Final Technical Report, LMSC-D352890, Lockheed Palo Alto Research Laboratory, Palo Alto, California, 31 Aug 1973

3. P. D. Thomas and H. M. Musal, A Theoretical Study of Laser-Target Interaction, First Semiannual Technical Report, LMSC-D313142, Lockheed Palo Alto Research Laboratory, Palo Alto, California, 22 Dec 1972

4. C. Walters, "Experimental Studies of LSDW Initiation," presented at the DoD Laser Effects/Hardening Conference, Monterey, California, 23–26 Oct 1973

5. R. B. Hall, W. E. Maher, and P. S. P. Wei, An Intestigation of Laser Supported Detonation Waves, Vol. 1 – "Experimental," Report No. D180-15336-1, Boeing Aero-Aerospace Corp., Seattle, Washington, Feb 1973

6. R. B. Hall, W. E. Maher, and P. S. P. Wei, An Investigation of Laser-Supported Detonation Waves, Report No. AFWL-TR-73-28, prepared by Boeing Aerospace Co., published by Air Force Weapons Laboratory, Kirtland AFB, New Mexico, Jun 1973

7. E. L. Klosterman, S. R. Byron, and J. F. Newton, Laser-Supported Combination Wave Study, Report No. 73-101-3, Math. Sciences North West, Inc., Seattle, Washington, Dec 1973

8. E. L. Klosterman and S. R. Byron, Experimental Study of Subsonic Laser Absorption Waves, AFWL-TR-74-003, MSNW Report No. 73-101-4, Math. Sciences North West, Inc., Seattle, Washington, Dec 1973

9. R. W. Conrad, "Plasma Initiation and Propagation With a High Power, CW, CO_2 Laser," presented at the Workshop on Laser-Induced Combustion Waves held at MSNW, Seattle, Washington, 5–6 Dec 1972

10. A. Edwards, N. Ferriter, J. A. Fleck, Jr., and A. M. Winslow, A Theoretical Description of the Interaction of a Pulsed Laser and a Target in an Air Environment, UCRL-51489, Lawrence Livermore Laboratory, University of California, Livermore, California, Nov 1973

11. E. L. Klosterman, Private Communication

12. W. W. Dolan and W. P. Dyke, "Temperature-and-Field Emission of Electrons From Metals," Phys. Rev., Vol. 95, No. 2, Jul 15, 1954, pp. 327–332

13. E. L. Murphy and R. H. Good, Jr., "Thermionic Emission, Field Emission, and the Transition Region," Phys. Rev., Vol. 102, No. 6, Jun 15, 1956, pp. 1464–1473

14. R. F. Harrington, Time-Harmonic Electromagnetic Fields, New York, McGraw-Hill, 1961

15. J. P. Jackson and P. E. Nielsen, "Role of Radiative Transport in the Propagation of Laser Supported Combustion Waves," AIAA paper No. 74–228, AIAA 12th Aerospace Sciences Meeting, Washington, D.C., Jan 1974

16. A. A. Boni and F. Y Su, "Subsonic Propagation of Laser Supported Waves," AIAA paper No. 74-567, AIAA 7th Fluid and Plasma Dynamics Conference, Palo Alto, California, Jun 1974